

## OUR SUN. III. PRESENT AND FUTURE

I.-Juliana Sackmann,<sup>1</sup> Arnold I. Boothroyd,<sup>2</sup> and Kathleen E. Kraemer<sup>1,3</sup>

## ABSTRACT

Self-consistent evolutionary models were computed for our Sun, using Los Alamos interior opacities and Sharp molecular opacities, starting with contraction on the Hayashi track, and fitting the observed present solar  $L$ ,  $R$ , and  $Z/X$  at the solar age. This resulted in presolar  $Y = 0.274$ , and  $Z = 0.01954$ , and in present solar  $^{37}\text{Cl}$  and  $^{71}\text{Ga}$  neutrino capture rates of 6.53 and 123 SNU, respectively.

We explored the Sun's future. While on the hydrogen-burning main sequence, the Sun's luminosity grows from  $0.7 L_{\odot}$ , 4.5 Gyr ago, to  $2.2 L_{\odot}$ , 6.5 Gyr from now. A luminosity of  $1.1 L_{\odot}$  will be reached in 1.1 Gyr, and  $1.4 L_{\odot}$  in 3.5 Gyr; at these luminosities, Kasting predicts "moist greenhouse" and "runaway greenhouse" catastrophes, respectively, using a cloud-free climate model of the Earth; clouds could delay these catastrophes somewhat. As the Sun ascends the red giant branch (RGB), its convective envelope encompasses 75% of its mass (diluting remaining  $^7\text{Li}$  by two orders of magnitude;  $^4\text{He}$  is enhanced by 8%,  $^3\text{He}$  by a factor of 5.7,  $^{13}\text{C}$  by a factor of 3, and  $^{14}\text{N}$  by a factor of 1.5). The Sun eventually reaches a luminosity of  $2300 L_{\odot}$  and a radius of  $170 R_{\odot}$  on the RGB, shedding  $0.275 M_{\odot}$  and engulfing the planet Mercury. After the horizontal branch stage (core helium burning), the Sun climbs the asymptotic giant branch (AGB), encountering four thermal pulses there; at the first thermal pulse, the Sun reaches its largest radial extent of  $213 R_{\odot}$  (0.99 AU), which is surprisingly close to Earth's present orbit. However, at this point the Sun's mass has been reduced to  $0.591 M_{\odot}$ , and the orbits of Venus and Earth have moved out to 1.22 and 1.69 AU, respectively—they both escape being engulfed. The Sun reaches a peak luminosity of  $5200 L_{\odot}$  at the fourth thermal pulse. It ends up as a white dwarf with a final mass of  $0.541 M_{\odot}$ , shifting the orbits of the planets outward such that Venus and Earth end up at 1.34 and 1.85 AU, respectively. These events on the AGB are strongly mass-loss dependent; somewhat less mass loss can result in engulfment of Venus, or even Earth. Our preferred mass loss rate was a Reimers wind with a mass loss parameter  $\eta = 0.6$  normalized from inferred mass loss in globular cluster stars. For reasonable mass loss rates ( $0.8 > \eta > 0.4$ ), the Sun's final white dwarf mass is between  $0.51$  and  $0.58 M_{\odot}$ .

The Sun spends 11 Gyr on the main sequence, 0.7 Gyr cooling toward the RGB, 0.6 Gyr ascending the RGB, 0.1 Gyr on the horizontal branch, 0.02 Gyr on the early AGB, 0.0004 Gyr on the thermally pulsing AGB, and 0.0001 Gyr on the traverse to the planetary nebula stage (the last three of these time scales depend sensitively on the amount of mass loss).

*Subject headings:* solar system: general — stars: evolution — Sun: general — Sun: interior

---

<sup>1</sup> W. K. Kellogg Radiation Laboratory 106-38, California Institute of Technology, Pasadena, CA 91125.

<sup>2</sup> Canadian Institute for Theoretical Astrophysics, University of Toronto, 60 St. George Street, Toronto, Ontario, Canada M5S 1A7.

<sup>3</sup> Now at Department of Astronomy, Boston University, 725 Commonwealth Avenue, Boston, MA 02215.

## 1. INTRODUCTION

Our Sun is the star for which the greatest wealth of observations exists. As a result, tremendous efforts have been made to understand the Sun's interior structure and history (for a review, see, e.g., Bahcall & Ulrich 1988; Bahcall & Pinsonneault 1992*a*). Relatively little work has focused on the future of our Sun and its final fate. Following our work on standard solar models (Sackmann, Boothroyd, & Fowler 1990; hereafter Paper I) and on nonstandard solar models with early main-sequence mass loss (Boothroyd, Sackmann, & Fowler 1991; hereafter Paper II), we could not resist exploring the Sun's future by continuing our models beyond the commonly-calculated main sequence stage. We followed the Sun as it became a red giant (undergoing considerable mass loss); as it encountered a violent helium core flash; as it underwent quiescent helium burning in its core; as it became a red giant for the second time while traversing the asymptotic giant branch (AGB), where it encountered violent repetitive helium shell flashes, and again suffered considerable mass loss; and as it left the AGB (when practically no hydrogen envelope remained outside the degenerate core) on its way to becoming the nucleus of a planetary nebula (and eventually a white dwarf). Of key interest are the time scales of the various stages, the luminosity increases, the solar mass as a function of time, changes in the surface chemical composition, and whether or not the Sun eventually engulfs the inner planets (especially the Earth).

Recently Jørgensen (1991, 1992) estimated the future of the Sun, using published sets of stellar evolutionary tracks from the literature. Since none of these published tracks was designed to fit the composition and mixing length required for the Sun, the existing data had to be interpolated, extrapolated, and sometimes shifted. Jørgensen (1991) pointed out that self-consistent models designed to match the Sun would be much more reliable.

The results presented here are full self-consistent stellar evolutionary models, starting from the pre-main-sequence contraction phase. The models had the (observed) solar composition, with the initial helium abundance and mixing length parameter tuned to make the models match the present solar luminosity and radius. Details concerning the input physics and mass loss are discussed in § 2. Our results are presented in § 3, and conclusions in § 4.

## 2. METHODS

Our previous solar models (papers I and II) started from homogeneous models near the main sequence, with internal energy generation coming from nuclear burning (rather than gravitational contraction). The models described in this paper start earlier, as homogeneous models contracting on the pre-main-sequence Hayashi track, prior to the ignition of nuclear burning. This change results in no significant difference after one reaches the main sequence, except that it allows computation of pre-main-sequence lithium depletion.

### 2.1. Values of $M_{\odot}$ , $R_{\odot}$ , $L_{\odot}$ , and $t_{\odot}$

We have made minor changes in our adopted values of the solar mass, luminosity, and radius. As described in Guenther *et al.* (1992), the solar mass is  $M_{\odot} \equiv 1.9891 \times 10^{33}$  g, with an uncertainty of 0.02% (Cohen & Taylor 1986), and the solar radius at an optical depth of  $\tau = 2/3$  is slightly reduced from the value of  $6.96 \times 10^{10}$  cm measured at  $\tau = 0.001$ , namely  $R_{\odot} \equiv 6.9598 \times 10^{10}$  cm (Ulrich & Rhodes 1983). Averaging recent accurate measurements of the solar constant (Willson & Hickey 1977; Willson, Duncan, & Geist 1980; Hickey & Alton 1983) yields a value of  $1370 \text{ W m}^{-2}$ , with an uncertainty of  $2 \text{ W m}^{-2}$  implied by the scatter in the data (the formal errors quoted in these papers would imply an uncertainty only half as large); this implies a solar luminosity of  $L_{\odot} \equiv 3.854 \times 10^{33} \text{ erg s}^{-1}$ , with an uncertainty of 1.5%. The age of the meteorites has been measured to be 4.55 Gyr (see, e.g., Wasserburg *et al.* 1977; Wasserburg, Papanastassiou, & Lee 1980). The meteorites presumably formed during the pre-main-sequence contraction

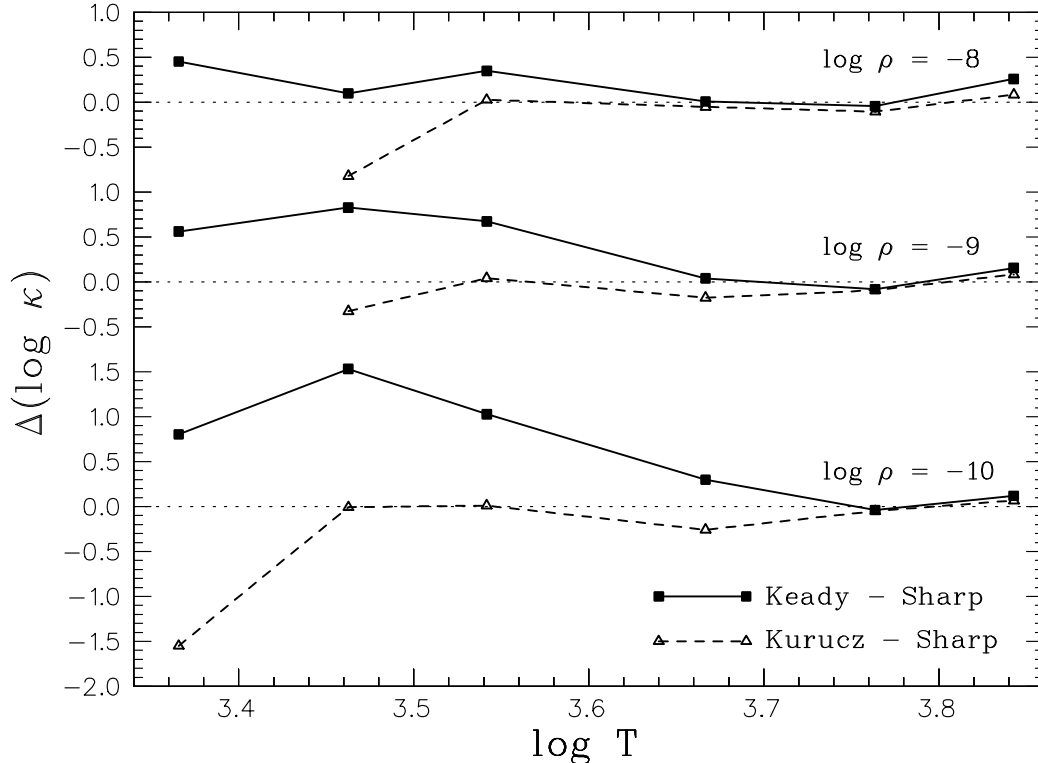


Fig. 1.—Comparison of the Sharp (1992) molecular opacities with those of Keady (1985) and Kurucz (1990) at densities and temperatures applicable to the outer regions of red giant stars.

phase of the Sun, while it still had a dense accretion disk. We therefore take the time from our initial pre-main-sequence model to the present Sun to be 4.55 Gyr (corresponding to a *main sequence* age of 4.50 to 4.52 Gyr, as discussed in § 3.2.2). The earliest contraction phase on the upper Hayashi track is very fast (most time being spent after the star approaches the base of the Hayashi track), so that it does not matter exactly where on the Hayashi track one starts. (Note that uncertainties in the solar age have very little effect on solar models: see Paper I.)

## 2.2. Opacities

In the interior, we continued to use the Los Alamos Opacity Library (LAOL) opacities obtained from Keady (1985). At low temperatures, we had previously used the molecular opacities also supplied by Keady; however, for the present work we modified these molecular opacities at low temperatures and densities in order to accord with the more recent molecular opacities of Sharp (1992), as discussed below. As in our previous work, we interpolated among these tables in metallicity  $Z$  and hydrogen abundance  $X$  in order to obtain the opacity corresponding to the composition at each point in our models: the opacity  $\kappa$  was interpolated linearly in  $Z$  and in  $X$ .

Keady (1985) supplied us with Los Alamos tables for hydrogen-rich ( $X = 0.7$ ) and hydrogen-poor ( $X = 0$ ) mixtures, for metallicities  $Z = 0.02$ ,  $Z = 0.001$ , and  $Z = 0.0001$ . Opacities due to a number of molecules were included, namely  $\text{H}^-$ ,  $\text{H}_2$ ,  $\text{H}_2^+$ ,  $\text{H}_2^-$ ,  $\text{H}_2\text{O}$ ,  $\text{N}_2$ ,  $\text{CO}$ , and  $\text{CN}$ .

The molecular opacities of Sharp (1992) are a considerable improvement over the earlier LAOL molecular opacities sent to us by Keady (1985). Sharp considered many more molecules, as well as improving the opacity calculations for individual molecules, including opacities of the triatomic molecules  $\text{H}_2\text{O}$  and  $\text{CO}_2$ . However, the Sharp opacities were only computed for solar composition and for an enhanced-CNO composition, and were only reliable below  $\log T \sim 3.8$  (since he ignored atomic lines that become important

at higher temperatures). Therefore the Sharp opacities, though of great interest for the low-temperature regions, have insufficient range in temperature and composition to replace entirely the Keady molecular opacities.

We compared the Sharp (1992) molecular opacities to the Keady (1985) opacities, and also to recent molecular opacities of Kurucz (1990), as shown in Figure 1. Kurucz computed diatomic molecular opacities in great detail, but included no triatomic molecules; thus his opacities are much too low at low temperatures where H<sub>2</sub>O opacity becomes important (i.e., at  $\log T \lesssim 3.5$  for densities  $\log \rho \lesssim -8$ ). From Figure 1, one can see that the Sharp and Kurucz opacities agree quite well above these temperatures. However, the Keady opacities are far larger than either the Sharp or the Kurucz opacities for  $\log T \lesssim 3.7$  and  $\log \rho \lesssim -8$ . From these comparisons, we concluded that the Sharp opacities were the most reliable of these three for the temperature range  $3.36 < \log T \lesssim 3.7$ . Thus we shifted the Keady hydrogen-rich molecular opacity tables for all three metallicities by the difference between the Sharp and Keady tables for the solar composition, for  $\log T < 3.7$  and  $\log \rho < -7$ ; the resulting opacity tables we refer to as our “Sharp” opacity tables. (Note that the lowest temperatures are reached only in the outer regions of red giants, which have very low density.) This modification might result in some error at low metallicities (though hopefully still an improvement over the Keady tables), but should be fairly reliable for solar composition.

Note that changes in the molecular opacities have very little effect on models of the present Sun (one must merely change the mixing length parameter  $\alpha$  to compensate: see Paper I). However, there is an effect on the pre-main-sequence and post-main-sequence red giant phases (Sackmann & Boothroyd 1991).

### 2.3. Presolar Helium and the Mixing Length

For a given presolar helium abundance  $Y$  and mixing length parameter  $\alpha$ , one can compute the solar evolution from time zero up to the solar age, obtaining the luminosity and radius of the model at the solar age. The value of  $Y$  affects both the luminosity and the radius at the solar age, while  $\alpha$  affects primarily the radius. By adjusting the values of  $Y$  and  $\alpha$ , one proceeds to match the observed solar luminosity and radius. The resulting values of  $Y$  and  $\alpha$  depend to some extent on the details of one’s models, such as the opacities and (to a lesser extent) the equation of state and nuclear reaction rates. With the present stellar evolution code, we obtained  $Y = 0.274$  and  $\alpha = 2.10$ , where we used for  $Z/X$  the observed value of 0.027665 from Grevesse (1984), resulting in  $Z = 0.01954$ .

### 2.4. Mass Loss

For mass loss during red giant stages, we used the Reimers (1975) parameterization, namely

$$\dot{M} = -\eta (4 \times 10^{-13}) \frac{LR}{M} = -\eta (1.34 \times 10^{-5}) \frac{L^{3/2}}{M T_e^2}, \quad (1)$$

where  $M$ ,  $L$ , and  $R$  are in solar units,  $\dot{M}$  in  $M_\odot \text{ yr}^{-1}$ , and  $T_e$  in kelvins;  $\eta$  is the mass-loss parameter. We applied this mass loss only for the low effective temperatures characteristic of a red giant, namely  $\log T_e < 3.71$ .

Kudritzki & Reimers (1978) found that a value of  $\eta \approx 1.4$  was in agreement with observed stellar winds of high-luminosity red giants. However, Renzini (1981) modeled lower-luminosity stars, namely low-metallicity ( $Z = 0.001$ ) stars of mass  $0.85 M_\odot$ , and found that a value of  $\eta \approx 0.4$  was necessary to match the observed extent in effective temperature of the horizontal branch in globular clusters. The difference in luminosity between the main-sequence turnoff and the horizontal branch required a main-sequence mass of  $0.85 M_\odot$ , while the effective temperatures on the horizontal branch require a mass of about  $0.65 M_\odot$  there, for a total mass loss of  $0.2 M_\odot$  on the RGB of a low-metallicity star of initial mass  $0.85 M_\odot$ . The precise value of  $\eta$  obtained in this way depends on one’s low-temperature opacities (and on the mixing length parameter  $\alpha$ ,

which is determined by a standard solar model on the main sequence, but which could in theory be different on the RGB).

We recalculated a  $0.85 M_{\odot}$ ,  $Z = 0.001$ ,  $Y = 0.24$  case with our “Sharp” opacity tables and the above-derived value of  $\alpha = 2.1$ . We found that a mass-loss parameter of  $\eta \approx 0.6$  was required in order to obtain a total mass loss of  $0.2 M_{\odot}$  along the RGB for this star. Thus  $\eta = 0.6$  is our *preferred* mass-loss parameter value for our solar model. However, we also explored other mass-loss cases, namely  $\eta = 0.4$  (as a lower limit to mass loss) and  $\eta = 1.4$  (as derived for solar metallicity but higher-luminosity stars). It should be noted that there are indications that the Reimers (1975) red giant mass-loss parameterization underestimates the luminosity dependence of mass loss, as shown by the above-described  $\eta$ -discrepancy and by the fact that observed mass-loss rates at the highest-luminosity tip of the AGB are much higher than the Reimers rate would indicate (see, e.g., de Jong 1983). Since the Sun is a relatively low-mass star, it never reaches AGB luminosities much higher than those attained on the RGB, and therefore the value of  $\eta = 1.4$  presumably greatly overestimates the amount of solar mass loss. One should also note that uncertainties in the *luminosity dependence* of mass loss should have relatively little effect, since the Sun’s AGB luminosity is similar to the RGB luminosity for which the value of  $\eta = 0.6$  was derived.

### 2.5. Other Details of the Code

Our stellar evolutionary program is described in some detail in Boothroyd & Sackmann (1988), including a description of semiconvection and of the gray atmosphere; see also Sackmann *et al.* (1990). Most nuclear rates are still taken from Caughlan & Fowler (1988), but two reaction rates have been changed: the  $^{17}\text{O}(p, \alpha)^{14}\text{N}$  and  $^{17}\text{O}(p, \gamma)^{18}\text{F}$  rates of Landré *et al.* (1990) were used, with parameters  $f_1 = 0.2$  (as they recommend) and  $f_2 = 0.1$  (which has no effect on the rates except at temperatures much higher than encountered here). Also, we have corrected an error in the  $p$ - $p$  chain branching ratio at  $^7\text{Be}$ , which had resulted in an 18% overestimate of the  $^7\text{Be}(p, \gamma)^8\text{B}$  branch. Since  $^7\text{Be}$  is on the high-temperature branch of the  $p$ - $p$  chain, correcting the error has no effect on the structure of the Sun, but it does reduce the predicted solar  $^8\text{B}$  neutrino flux of our models by 18% relative to the values quoted in our Papers I and II (see discussion in § 3.1).

The equation of state remains unchanged. Corrections to the ideal gas equation of state effectively apply about 60% of the Debye-Hückel correction in the main-sequence solar interior; one should note that Guenther *et al.* (1992) find that the recent “MHD” equation of state (Mihalas, Däppen, & Hummer 1988; Hummer & Mihalas 1988; Mihalas *et al.* 1990) contains effects partially canceling the Debye-Hückel effect.

## 3. RESULTS

### 3.1. The Present Sun

The Sun is presently on the main sequence, burning hydrogen quietly in its core; changes in the solar luminosity and radius are extremely slow, with time scales of billions of years. As discussed in § 2, our models predict a presolar helium abundance of  $Y = 0.274$  and a mixing length parameter of  $\alpha = 2.10$ , with  $Z = 0.01954$ . These values are slightly different from our previous values quoted in Paper I (namely,  $Y = 0.278$ ,  $\alpha = 2.07$ , and  $Z = 0.01943$ ), due to the changes in the opacities and time-zero starting point. Our model has a central temperature of  $T_c = 15.43 \times 10^6$  K, a central density of  $\rho_c = 145.7 \text{ g cm}^{-3}$ , and a central pressure of  $P_c = 2.269 \times 10^{17} \text{ erg cm}^{-3}$ . Nearly half the central hydrogen has been burned: the hydrogen mass fraction at the center is  $X_c = 0.3632$ , compared to the initial hydrogen mass fraction of  $X = 0.7064$ . These values are very similar to those quoted in our Paper I: the different starting point has very little effect. The same is true for the predicted conditions at the base of the envelope convective region: we find the mass coordinate  $M_r$  (i.e., the mass inside a sphere of radius  $r$ ) at the base of convection to be  $M_{ceb} = 0.9832 M_{\odot}$ , with temperature  $T_{ceb} = 1.959 \times 10^6$  K, density  $\rho_{ceb} = 0.134 \text{ g cm}^{-3}$ , pressure  $P_{ceb} = 3.51 \times 10^{13} \text{ erg cm}^{-3}$ ,

TABLE 1  
 Predicted Neutrino Fluxes ( $\text{cm}^{-2} \text{s}^{-1}$  at Earth) and Capture Rates (SNU)

Target	$p-p$	$pep$	${}^7\text{Be}$	${}^8\text{B}$	${}^{13}\text{N}$	${}^{15}\text{O}$	${}^{17}\text{F}$	${}^{18}\text{F}$	${}^3\text{He}-p$	Total
$\nu$ flux <sup>a</sup>	6.06+10	1.30+8	4.18+9	4.72+6	4.04+8	3.12+8	4.26+6	9.87+4	6.53+3	6.57+10
${}^7\text{Li}$	0	8.52	4.02	18.4	1.72	7.67	0.106	0	0.055	40.5
${}^{37}\text{Cl}$	0	0.208	1.00	5.00	0.069	0.212	0.0029	0	0.026	6.53
${}^{71}\text{Ga}$	71.5	2.80	30.6	11.5	2.50	3.62	0.050	0.00016	0.048	123.
${}^{81}\text{Br}$	0	0.98	7.65	12.7	0.59	1.14	0.016	0	0.059	23.2
${}^{98}\text{Mo}$	0	0	0	14.2	0	0	0	0	0.065	14.2
${}^{115}\text{In}$	473.	7.5	104	11.8	9.1	11.1	0.15	0.00088	0.040	616.

<sup>a</sup> Power-of-ten notation:  $6.06+10 \equiv 6.06 \times 10^{10}$ , etc.

and radius  $R_{ceb} = 0.741 R_{\odot}$ . This convective radius is somewhat further out than the value obtained from helioseismological observations, namely  $R_{ceb} = 0.713 \pm 0.003 R_{\odot}$  (Christensen-Dalsgaard, Gough, & Thompson 1991). However, it has been pointed out by Guenther *et al.* (1992) that  $R_{ceb}$  is lowered by about  $0.02 R_{\odot}$  by use of the more recent OPAL interior opacities of Iglesias & Rogers (1991) rather than the Los Alamos opacities. Proffitt & Michaud (1991) found that  $R_{ceb}$  is lowered by slightly less than  $0.02 R_{\odot}$  when one includes diffusion of hydrogen and helium, but that when the (slightly more uncertain) diffusion of heavier elements is considered as well, this effect is approximately cancelled, possibly even reversed to some extent. Bahcall & Pinsonneault (1992b) used OPAL opacities and considered hydrogen and helium diffusion, but *not* diffusion of heavier elements, and found  $R_{ceb} = 0.707 R_{\odot}$ . Thus including the improved OPAL opacities alleviates the  $R_{ceb}$  discrepancy considerably; the effect of diffusion is less clear.

The predicted present solar neutrino flux is shown in Table 1; the capture cross sections were taken from Bahcall & Ulrich (1988), as in Paper I. The predicted neutrino fluxes from individual reactions are within 1% of those quoted in Paper I, except for the  ${}^8\text{B}$  neutrino fluxes, which are decreased by 19% (due mostly to the corrected branching ratio discussed in § 2.5). The predicted (total)  ${}^{37}\text{Cl}$  capture rate is 6.53 SNU (as compared to 7.68 SNU in Paper I); the corrected  $p-p$  chain branching ratio at  ${}^7\text{Be}$  is responsible for reduction of about 1 SNU, with the difference in the pre-main-sequence starting point accounting for the remaining 0.1 SNU. The predicted (total)  ${}^{71}\text{Ga}$  capture rate is 123 SNU (as compared to 125 SNU in Paper I). Note that use of the Johnson *et al.* (1992) rate for  ${}^7\text{Be}(p, \gamma){}^8\text{B}$  would reduce the  ${}^8\text{B}$  neutrino flux by 6% compared to the Caughlan & Fowler (1988) rate used in our models (resulting in a total  ${}^{37}\text{Cl}$  capture rate of 6.2 SNU, rather than 6.5 SNU). On the other hand, both OPAL opacities and diffusion effects would result in higher central temperatures, and thus in higher predicted neutrino rates (Guenther *et al.* 1992; Proffitt & Michaud 1991; Bahcall & Pinsonneault 1992b). The use of OPAL opacities results in a central temperature increase of 1.6% according to Guenther *et al.* (1992), but only 0.8% according to Faulkner & Swenson (1992); since the  ${}^8\text{B}$  neutrino flux is proportional to  $T_c^{18}$  (Bahcall & Ulrich 1988), these  $T_c$  increases would result in increases of 33% or 15%, respectively, in the  ${}^8\text{B}$  neutrino flux. The other neutrino producing reactions are less temperature sensitive: for example, from Bahcall & Pinsonneault (1992b), the percentage increase in the  ${}^7\text{Be}$  neutrino rate is about half that of the  ${}^8\text{B}$  neutrino rate. One therefore may estimate that the OPAL opacities would result in total  ${}^{37}\text{Cl}$  capture rates of 8.4 or 7.4 SNU, respectively, for the  $T_c$  increases of Guenther *et al.* (1992) or of Faulkner & Swenson (1992). Including  ${}^4\text{He}$  diffusion increases the central temperature by 0.7%, 0.5%, or 0.3%, according to the results of Bahcall & Pinsonneault (1992b), Proffitt & Michaud (1991), or Cox, Guzik, & Kidman (1989), respectively, resulting in  ${}^8\text{B}$  neutrino increases of 12%, 10%, or 6%. Taking both OPAL opacities and  ${}^4\text{He}$  diffusion into account would thus be expected to increase our total  ${}^{37}\text{Cl}$  capture rate to a value in the range 7.8–9.3 SNU (or 7.4–8.9 SNU, if the Johnson *et al.*

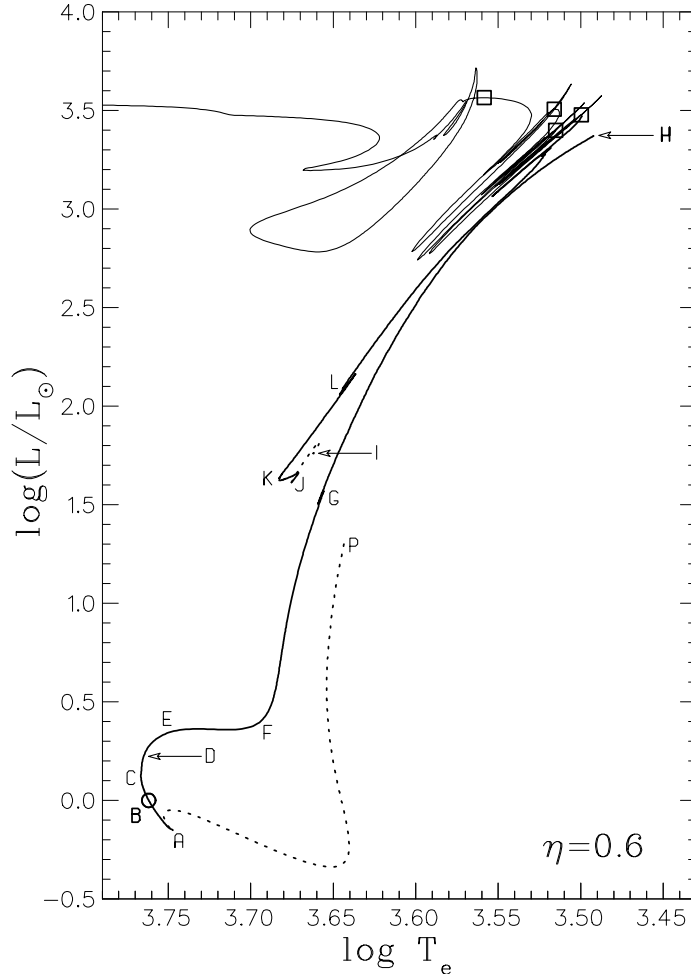


Fig. 2.—The Sun’s evolution in the HR diagram, from the pre-main-sequence starting point P until the post-AGB stage (at upper left). Dotted lines refer to the less-certain and less-important pre-main-sequence (P-A) and pre-ZAHB (I-J) stages. The circle at point B indicates the present Sun. The squares indicate the beginning of the four successive helium shell flashes on the AGB. The Reimers mass-loss parameter  $\eta = 0.6$  is our preferred case; see § 2.4. For an explanation of the stages delimited by the other letters, see § 3.2.

1992 rate were used). Bahcall & Pinsonneault (1992a) discussed in some detail uncertainties in the predicted solar neutrino rates due to uncertainties in the solar physics; their “total theoretical range” of uncertainty (effectively a  $3\sigma$  error) was about 38% for  $^{37}\text{Cl}$ , and about 14% for  $^{71}\text{Ga}$ . The observed  $^{37}\text{Cl}$  capture rate is only  $2.3 \pm 0.25$  SNU (Davis *et al.* 1990), and the observed  $^{71}\text{Ga}$  capture rate is  $(83 \pm 19 [\text{stat.}] \pm 8 [\text{syst.}])$  SNU (GALLEX collaboration 1992). The discrepancy between observed and predicted neutrino rates is most probably due to conversion of electron neutrinos into muon (or tau) neutrinos in the solar interior via the Mikheyev-Smirnov-Wolfenstein (MSW) effect (Mikheyev & Smirnov 1986; Wolfenstein 1978).

### 3.2. Solar Luminosity, and Time Scales

The Hertzsprung-Russell (HR) diagram of Figure 2 shows the various stages in the life of the Sun, in terms of its luminosity  $L$  and effective temperature  $T_e$ . Of key interest is the time that is spent in each of these stages, shown in Tables 2 and 3. We divide these stages as shown by the letters A through L, defined below.

TABLE 2

Characteristics of Our Standard Solar Model (with  $\eta = 0.6$ ) as a Function of Time <sup>a</sup>

Point	Time (Gyr)	$M$ ( $M_{\odot}$ )	$M_{ceb}$ ( $M_{\odot}$ )	$M_{X=0}$ ( $M_{\odot}$ )	$L$ ( $L_{\odot}$ )	$T_e$ (K)	$R$ ( $R_{\odot}$ )
P	0	1	0 <sup>b</sup>	–	19.95	4400	7.706
near-MS <sup>c</sup>	~ 0.031	1	0.9716	–	~ 0.893	~ 5600	~ 1.01
A	0.048	1	0.9750	–	0.7015	5586	0.8970
B	4.550	1	0.9832	–	1.0009	5779	1.0008
C	~ 7.56	1	~ 0.986	–	~ 1.33	5843	~ 1.13
D	9.37	1	0.9841	0.00005	1.67	5819	1.275
E	10.91	1	0.9643	0.0311	2.21	5617	1.575
F	11.64	0.9998	0.5516	0.1352	2.73	4902	2.30
min- $M_{ceb}$ <sup>d</sup>	12.088	0.9971	0.2445	0.2068	17.3	4664	6.38
G	~ 12.15	0.9935	~ 0.26	~ 0.240	~ 34.	~ 4540	~ 9.5
H	12.233	0.7249	0.46241	0.45945	2349.	3107	165.8
I	12.233	0.7249	0.56430	0.45945	57.7	4595	12.0
J	12.234	0.7249	0.60843	0.45945	41.0	4724	9.5
red-HB <sup>e</sup>	12.239	0.7241	0.59654	0.45951	45.9	4688	10.3
K	12.316	0.7133	0.64796	0.48187	42.4	4819	9.4
end-He-core <sup>f</sup>	12.344	0.7086	0.57975	0.48857	110.	4453	17.6
L	~ 12.345	~ 0.708	~ 0.57	~ 0.49	~ 130.	~ 4375	~ 20.
pre-flash-1 <sup>g</sup>	12.365 066	0.59101	0.53302	0.52968	2999.	3160	180.3
post-flash-4 <sup>h</sup>	12.365 355	0.54545	0.53832	0.53770	5190.	3660	177.0
peak-flash-5 <sup>i</sup>	12.365 446	0.54137	0.54137	0.54082	90.	74 080	0.058

<sup>a</sup>  $M$  is the Sun’s total mass,  $M_{ceb}$  the mass coordinate at the base of the convective envelope, and  $M_{X=0}$  the mass coordinate at the base of the hydrogen-burning shell; see § 3.2 for an explanation of the time-points (P and A through F).

<sup>b</sup> The entire Sun is convective at this pre-main sequence starting point P.

<sup>c</sup> The Sun closely approaches the main sequence at this point.

<sup>d</sup> Deepest convective envelope on the red giant branch (first dredge-up is completed at this point).

<sup>e</sup> “Red edge” (coolest effective temperature) on the horizontal branch.

<sup>f</sup> Core helium exhaustion.

<sup>g</sup> Start of the first helium shell flash (note that the maximum radius of  $213.4 R_{\odot}$  is reached in the post-flash expansion).

<sup>h</sup> Maximum expansion immediately following the fourth shell flash: maximum luminosity is reached at this point.

<sup>i</sup> Peak of the fifth and final shell flash, during cooling towards white dwarf stage: computations terminated here.



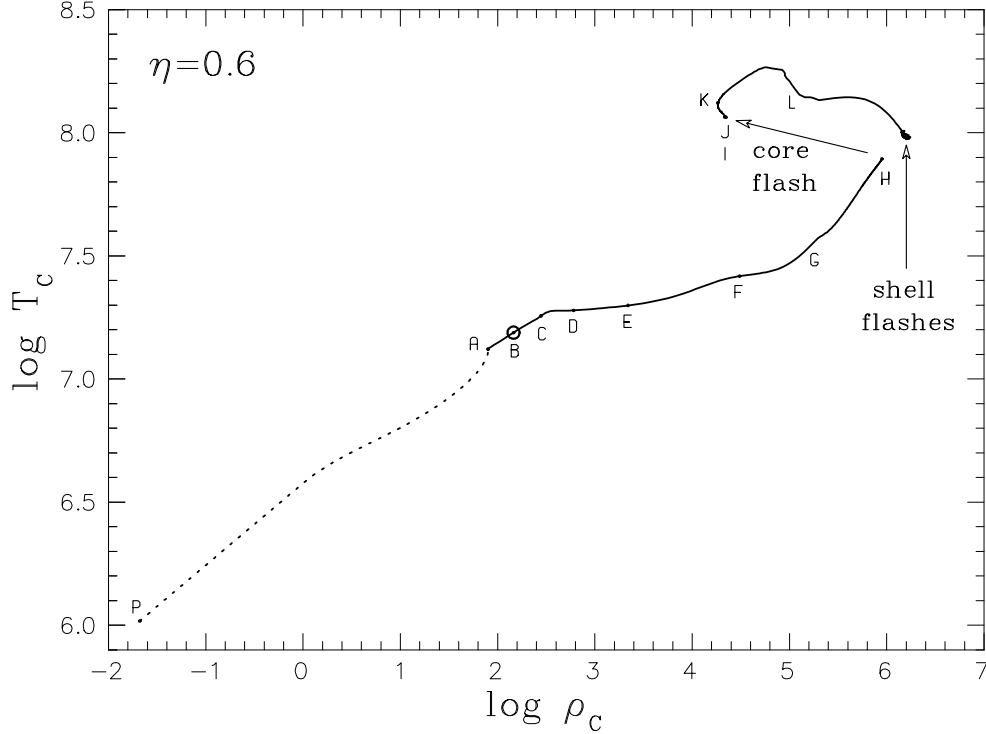


Fig. 3.—Evolution of the Sun’s central density and temperature, for our preferred case. Symbols have the same meaning as in Fig. 2.

### 3.2.1. The Sun’s Brief Youth: P-A

The zero-point in time for the Sun is our pre-main-sequence starting point P; there the Sun’s energy comes entirely from gravitational contraction, with no nuclear burning yet. The Sun descends rapidly in the HR diagram, dropping greatly in luminosity at nearly constant effective temperature for about 10 Myr; next, it approaches the main sequence more slowly (taking about 20 Myr), with less dramatic changes in luminosity (a factor of 2 increase), while the effective temperature increases by about 30%; the luminosity then drops slightly over the next 20 Myr, until it reaches a minimum at point A, which we define as the zero-age main sequence (ZAMS) (see Fig. 2). The Sun’s core contracts and heats considerably during this pre-main-sequence period, as shown in Figure 3, until hydrogen burning ignites in the center (at a

TABLE 3

Timescales and  $L$  and  $R$  Ranges For the Sun’s Major Evolutionary Stages

evolutionary stage	Time (Gyr)	$L$ range ( $L_{\odot}$ )	$R$ range ( $R_{\odot}$ )
A-E: main sequence	10.9	0.7 – 2.2	0.9 – 1.6
E-F: redwards traverse	0.7	2.3	1.6 – 2.3
F-H: red giant branch	0.6	2.3 – 2300	2.3 – 166
I-L: horizontal branch	0.11	44	~ 10
L to 1st flash: early AGB <sup>a</sup>	0.02	44 – 2000	10 – 130
thermally-pulsing AGB <sup>a</sup>	0.0004	500 – 5000	50 – 200
traverse to planetary nebula <sup>a</sup>	0.0001	3500	100 – 0.08

<sup>a</sup> These last three stages can be significantly affected by changes in mass loss.

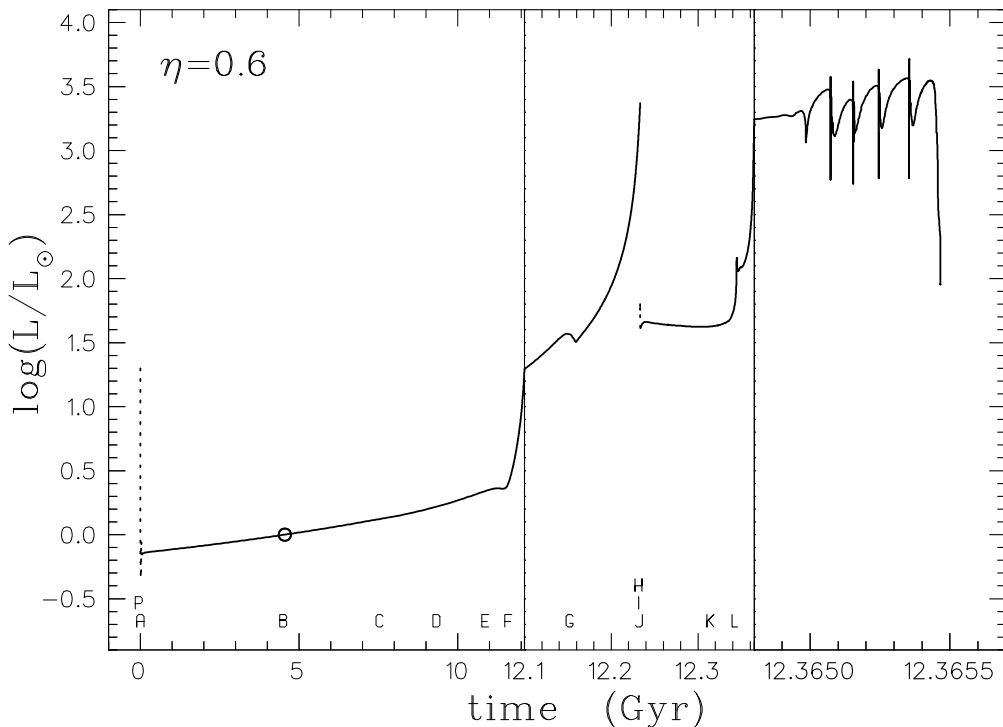


Fig. 4.—The Sun’s luminosity as a function of time, for our preferred case. Note the three different time scales, as the evolution speeds up. Symbols have the same meaning as in Fig. 2.

temperature of about  $12 \times 10^6$  K, and a density of about  $80 \text{ g cm}^{-3}$ ). At point A, the gravitational energy contribution has become negligible, and the Sun’s luminosity is derived from nuclear burning alone.

### 3.2.2. The Sun’s Quiet “Adulthood”: A-E

The main-sequence stage is a long-lived, quiescent stage when all of the Sun’s energy requirements are met by hydrogen burning in the core. Point B marks the present Sun, at an age of 4.55 Gyr (i.e., 4.50 Gyr since the ZAMS point A, or 4.52 Gyr since the Sun closely approached the main sequence). The value  $L_\odot$  is defined as the present solar luminosity, and  $R_\odot$  as the present solar radius (see § 2.1). Note that the Sun’s luminosity has changed relatively little since it reached the main sequence: at point A, it was 70% of the present value, increasing slowly and steadily since then (see Fig. 4). This long-lived and relatively stable epoch has been crucial to the existence of life on Earth; Figure 4 shows that we can anticipate an additional 7 Gyr of similarly slow luminosity increase.

Point C marks the hottest effective temperature the Sun will attain while in its main-sequence phase, 3 Gyr in the future. Point D marks the stage when hydrogen is exhausted at the very center of the Sun, 4.8 Gyr from now. Since there is still hydrogen left very near the center, slow evolution continues until point E, 6.4 Gyr from now, when a thick hydrogen-burning shell is developing and the Sun’s center begins to contract more rapidly (in order to provide the energy no longer provided there by nuclear burning). At point E, the end of the main sequence, the Sun’s luminosity is  $2.2 L_\odot$ . The total main-sequence lifetime is nearly 11 Gyr. However, even before the end of the “stable” main sequence, luminosities are reached that would have a catastrophic effect for life on Earth. Kasting (1988) has calculated that, for a cloud-free model, Earth would lose its water by way of a “moist greenhouse” at  $1.1 L_\odot$ , while the oceans would evaporate entirely at  $1.4 L_\odot$  due to a true “runaway greenhouse” (these luminosities will be reached 1.1 and 3.5 Gyr from now, respectively). Since clouds reduce the energy absorbed by the Earth, these catastrophes will be delayed until somewhat higher solar luminosities are attained, though presumably still before the end of the main sequence.

### 3.2.3. The Sun's Lively Old Age: E and Beyond

The central contraction after point E (due to the exhaustion of hydrogen fuel in the core) causes the hydrogen shell to get hotter and burn more strongly; this extra energy output results in the dramatic surface expansion which causes the Sun to become a red giant. The stage E-F, expansion at a nearly constant luminosity of  $2.3 L_{\odot}$ , takes about 0.7 Gyr. After reaching point F, at the base of the red giant branch (RGB), the expansion is even more rapid; but now the luminosity increases, while the effective temperature changes relatively little. The convective envelope reaches its deepest extent at a luminosity of  $17 L_{\odot}$  (see § 3.4); this leaves behind a composition discontinuity as convection retreats outward again. When the luminosity reaches about  $34 L_{\odot}$ , the hydrogen-burning shell encounters this discontinuity, resulting temporarily in a small reduction in the luminosity; this is defined as point G. Afterwards, the luminosity grows even faster, as can be seen from Figure 4: at the high-luminosity tip of the RGB (point H) the Sun reaches  $2349 L_{\odot}$ ! As will be discussed in § 3.3, the Sun suffers a considerable amount of mass loss as it approaches the tip of the RGB. The total time spent on the RGB is 0.6 Gyr, mostly spent at the lower luminosities.

The central contraction described in the above paragraph produces a hot, dense (electron-degenerate) core (see Fig. 3); since the ignition of hydrogen burning, the central temperature has increased by an order of magnitude, and the central density by four orders of magnitude. As the central temperature approaches  $10^8$  K, helium ignition takes place in the core. However, neutrino cooling (mostly from plasma neutrinos) is also nonnegligible as one approaches  $10^8$  K, being particularly strong at the densities of nearly  $10^6$  g cm $^{-3}$  that are reached at the Sun's center. This neutrino cooling causes the central temperature to grow less quickly than the temperature farther out in the core, so that helium ignition takes place off-center (at  $M_r \sim 0.13 M_{\odot}$ ).

Normally, when excess nuclear burning dumps energy into a star, the resulting expansion causes it to cool: this is a stable situation, since cooling reduces the nuclear energy generation, so that the perturbation is damped. However, under degenerate conditions, the excess energy goes into internal energy (lifting the degeneracy) and not into expansion, and the temperature increases; this leads to a nuclear runaway, which terminates only when the degeneracy has been lifted. Thus the helium ignition which takes place at point H results in the violent helium core flash: helium-burning energy generation rates of order  $10^{10} L_{\odot}$  are reached. However, this energy goes into lifting the degeneracy, and subsequent core expansion; there is no surface luminosity increase. In fact, the opposite occurs: the surface luminosity declines greatly (nearly two orders of magnitude), because the core expansion causes the surrounding hydrogen-burning shell (which has been supplying all the surface luminosity) to cool and thus to generate less energy. This initial decline is quite rapid (about  $10^4$  yr), but it is followed by roughly a million years of luminosity oscillations before the Sun settles down to quiet core helium burning on the horizontal branch (see, e.g., Thomas 1967; Despain 1981).

In previous work on low-mass stars (Boothroyd & Sackmann 1988), we have computed through the helium core flash for central-ignition cases. However, the present case of off-center ignition is more difficult to handle computationally, and we felt that it was not worth the trouble, considering that there are hardly any observational effects, and that relatively little core helium is burned in the core flash. Therefore we “jumped over” the core flash (see arrow in Fig. 3), restarting with a non-degenerate, quietly burning helium core at point I (and converting 3% of the core helium into carbon, as expected from the core flash; Boothroyd & Sackmann 1988). The model quickly settles down to the zero-age horizontal branch (ZAHB) at point J.

For the Sun, there is only a very small horizontal branch in the HR diagram, from J to K (see Fig. 2). The Sun remains at a nearly constant luminosity of about  $44 L_{\odot}$  for about 0.1 Gyr (i.e., about 1% as long as the stable main-sequence epoch). As the helium abundance in the Sun's core becomes small, the Sun's center contracts and heats more rapidly in order to maintain nuclear burning with a smaller fuel supply; this causes the hydrogen shell to contract, heat, and burn more strongly, driving the luminosity up rapidly just before core helium is exhausted. At point L helium is exhausted in the core, and helium burning is ignited

in a surrounding shell, while hydrogen continues to burn in a shell surrounding the hydrogen-exhausted core—the Sun has become a double-shell-burning star. There is a dip in the surface luminosity as the ignition of the helium-burning shell causes expansion and cooling of the hydrogen-burning shell (see Fig. 4). As the helium-burning shell burns its way towards the hydrogen-burning shell, the latter heats up again and the surface luminosity increases. This is the early AGB (E-AGB) phase, lasting 0.02 Gyr.

The carbon-oxygen core contracts, since there is no nuclear burning to support it. Normally, this contraction would result in heating of the core; however, neutrino energy losses have become large enough that the central temperature declines instead (see Fig. 3); the core eventually becomes degenerate. As the core contracts, it “squeezes” the burning shells around it. Eventually, another nuclear instability occurs, resulting in the violent repetitive helium shell flashes (also called thermal pulses): this stage is called the thermally pulsing AGB (TP-AGB). Helium shell flashes begin when the shell is thin enough that extra nuclear energy generation can cause only local expansion, with no pressure drop. Temperature then must rise as the local density falls, leading to a nuclear runaway that is quenched only when the shell has expanded sufficiently. This instability repeats after the helium shell has contracted again. Although the helium shell flashes are violent, with peak energy generation rates of order  $10^6 L_{\odot}$ , the surface luminosity varies by less than an order of magnitude. The surface luminosity first drops rapidly as expansion of the helium shell causes the extinction of the hydrogen-burning shell (this takes about 200 yr). The luminosity next increases as flash-produced energy reaches the surface (taking about 400 yr), then declines more slowly ( $10^4$  yr) as the helium shell flash is quenched. Finally, the luminosity slowly grows again as the hydrogen shell reignites, until the next flash occurs, about  $10^5$  yr later. Our preferred solar model encounters four of these helium shell flashes while on the TP-AGB, which lasts 0.0004 Gyr.

The Sun suffers considerable mass loss again on the AGB. When there is practically no envelope left outside the core, the Sun leaves the AGB; the effective temperature increases from about 4000 K to about 120 000 K at a nearly constant luminosity of about  $3500 L_{\odot}$ . Our model took about  $10^5$  yr to traverse the HR diagram from the fourth flash to the maximum effective temperature; this time scale is an upper limit, since we did not include mass loss during this stage (mass loss would speed up this stage of evolution). During this high-temperature stage, surrounding material shed from the Sun on the AGB becomes ionized, showing up as a planetary nebula. The Sun then cools and drops in luminosity, proceeding more and more slowly as it approaches the white dwarf stage. There is a small but nonnegligible chance that a final helium shell flash will occur during this descent toward becoming a white dwarf, and in fact our preferred solar model happened to encounter such a final shell flash. Since our code was not designed to handle a shell flash at this stage, we had to terminate the computations there (see Fig. 5). Presumably such a final shell flash would drive the Sun temporarily to larger luminosities and radii, before it finally settles down as a white dwarf. Iben *et al.* (1983) computed approximately the effects of such a final shell flash, finding that their model briefly became a red giant again. However, the peak helium flash strength  $L_{\text{He}}$  of their model was nearly  $10^8 L_{\odot}$  (Iben 1982), considerably greater than that of our Sun (which reached only  $L_{\text{He}} \sim 10^6 L_{\odot}$ ), and thus the Sun’s temporary expansion due to a final shell flash might not be nearly so dramatic. As discussed by Iben *et al.* (1983), there is only a 10% chance of encountering such a final helium shell flash; and in fact, our other solar models did not encounter such a final flash.

### 3.3. *The Sun’s Mass Loss*

There are two epochs in the Sun’s life when it becomes a red giant and major amounts of mass loss occur. The first is the RGB stage: most mass loss during this stage takes place near the tip of the RGB when the luminosity and radius are largest (reaching roughly  $2300 L_{\odot}$  and  $170 R_{\odot}$ , respectively). A peak mass-loss rate of  $\dot{M} = 1.3 \times 10^{-7} M_{\odot} \text{ yr}^{-1}$  is reached. The Sun has been reduced to a mass of  $0.725 M_{\odot}$  by the time the mass loss essentially stops (due to the helium core flash, which causes the luminosity to decrease).

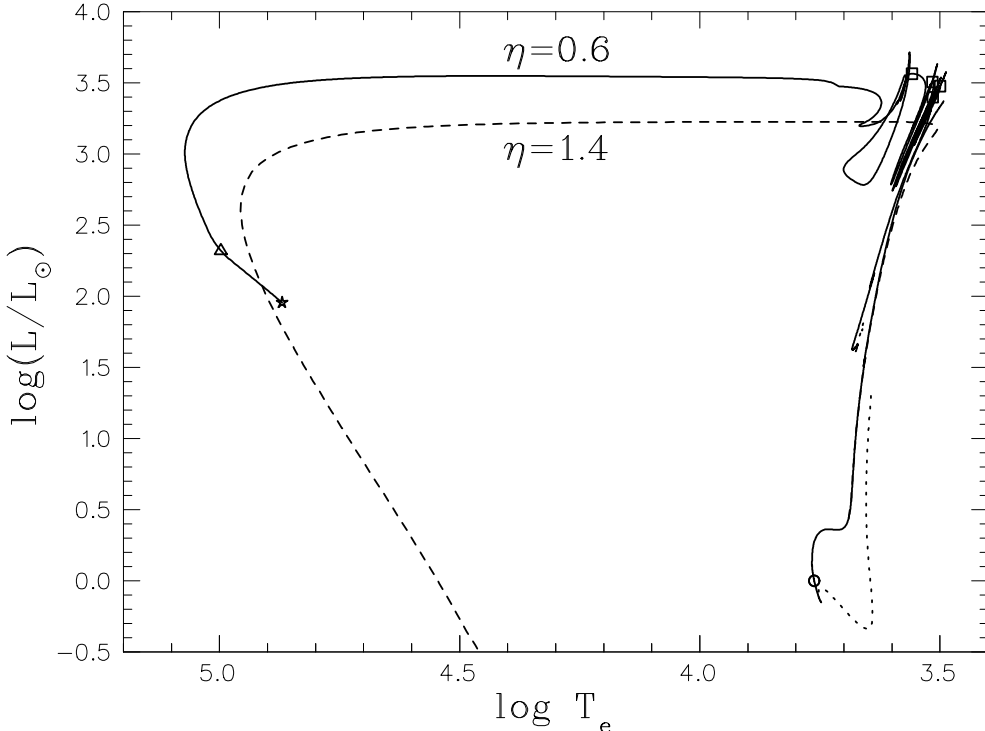


Fig. 5.—The Sun’s evolution in the HR diagram, from the pre-main-sequence stage to the pre-white dwarf stage. For our preferred mass-loss case (*solid curve*:  $\eta = 0.6$ ), the triangle indicates the beginning of the final helium shell flash, and the star its peak, where computations were terminated. The dashed curve shows our extreme mass-loss case ( $\eta = 1.4$ ), which leaves the RGB to become a helium white dwarf.

The second major mass-loss epoch occurs on the AGB, when the Sun again reaches very large luminosities and radii. During this stage, almost all the remaining envelope outside the hydrogen-burning shell is removed, stripping the Sun down to a mass of  $0.541 M_{\odot}$ . Nearly half the Sun’s initial mass has been lost. (Peak mass-loss rates of roughly  $\dot{M} = 2.5 \times 10^{-7} M_{\odot} \text{ yr}^{-1}$  are attained.) For details of the Sun’s mass as a function of time, see Figure 6a.

The above mass-loss results represent our preferred solar model, with the Reimers (1975) mass-loss parameter  $\eta = 0.6$  (obtained by normalizing to observed globular cluster horizontal branch positions, as discussed in § 2.4). However, because of the key importance of mass loss, we have also explored two other extreme mass-loss cases, namely  $\eta = 1.4$  and  $0.4$ .

The  $\eta = 1.4$  value is that obtained from observations of high-luminosity solar-metallicity red giants, and should be considered an upper limit for a lower-luminosity case such as the Sun (see § 2.4). Figure 6b shows that with this larger amount of mass loss all of the hydrogen envelope is lost on the RGB, before central helium ignition can take place. This case does not reach the tip of the RGB, and thus never encounters the horizontal branch or the AGB: as shown in Figure 5, it leaves the RGB to become a rather low-mass white dwarf, of mass  $0.434 M_{\odot}$ . Note that this white dwarf consists mainly of helium, rather than the carbon-oxygen white dwarf resulting from our preferred solar model.

We also computed a low mass-loss case, with  $\eta = 0.4$ . This case behaves similarly to our preferred solar model, except that it loses less mass on the RGB ( $0.171 M_{\odot}$  rather than  $0.275 M_{\odot}$ ), and lasts slightly longer on the AGB, encountering 10 helium shell flashes there rather than four. Its final mass is slightly larger, namely  $0.576 M_{\odot}$  (rather than  $0.541 M_{\odot}$ ): see Figure 6c.

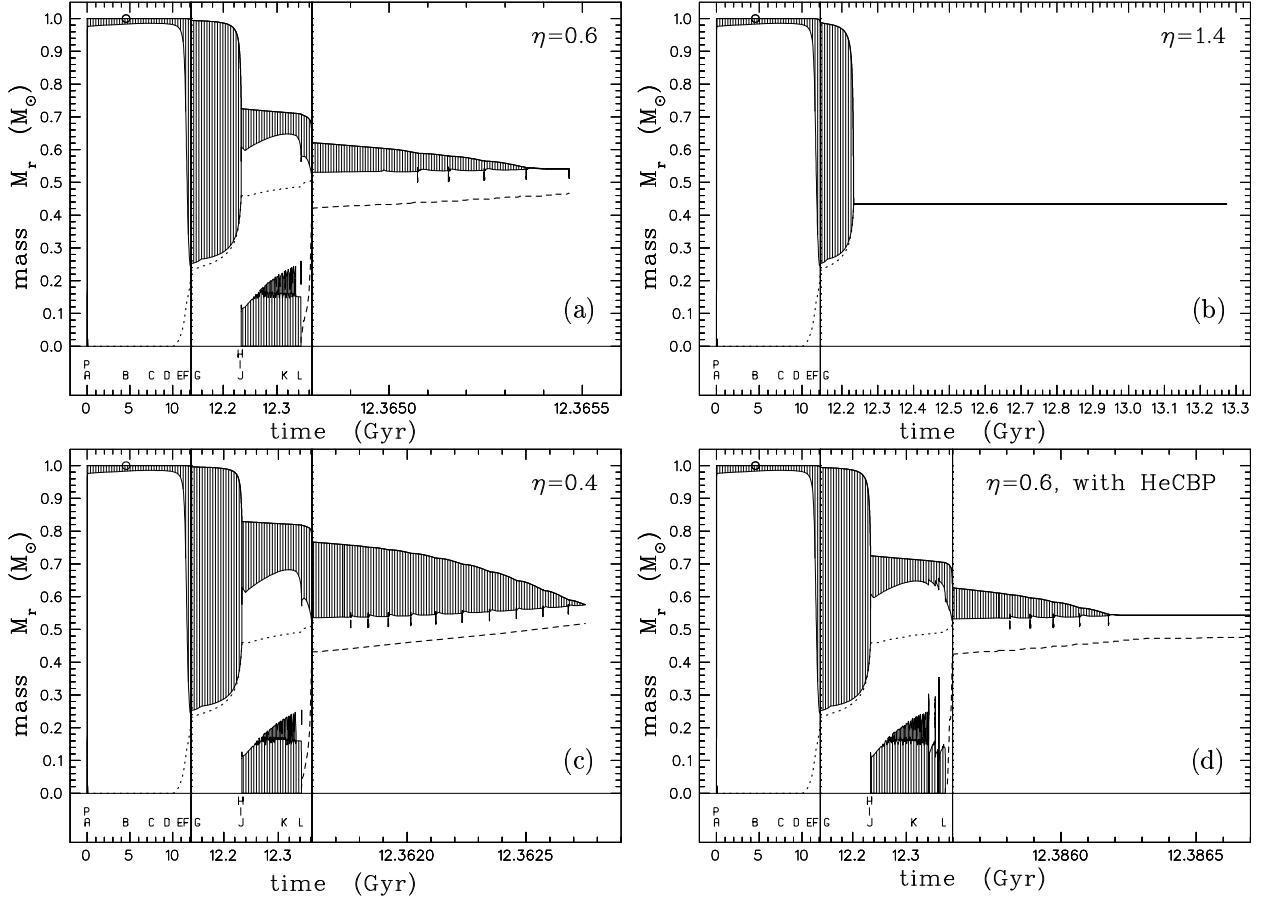


Fig. 6.—The Sun’s total mass and its convective regions, as a function of time. (a) Our preferred mass-loss case, with Reimers (1975) mass-loss parameter  $\eta = 0.6$ ; (b) our extreme mass-loss case, with  $\eta = 1.4$ ; (c) our low mass-loss case, with  $\eta = 0.4$ ; (d) our preferred mass-loss case ( $\eta = 0.6$ ), but with convective helium core breathing pulses. The heavy uppermost line gives the Sun’s total mass; the hatched region below it shows the extent of the convective envelope. The hatched region at the bottom shows core convection (associated with core helium burning), with the darker hatched region showing the semiconvective region (generally connected to the convective core). The dotted line shows the bottom of the hydrogen-burning shell, while the dashed line shows the bottom of the helium-burning shell. The five short vertical lines on the right are short-lived convective regions driven by the helium shell flashes, reaching from the center of the helium-burning shell almost (but not quite) to the hydrogen-burning shell. The circle refers to the present Sun; the symbols have the same meaning as in Fig. 2.

### 3.4. Convection and Semiconvection

Figure 6a also shows the convective regions in the Sun (hatched regions), as a function of time. On the early part of the pre-main-sequence (point P and a short period thereafter), the Sun is completely convective, as shown by the vertical line extending from the center to the surface at point P in Figure 6a. As the Sun gets closer to the main sequence, this convective region retreats toward the surface, until less than 3% of the Sun’s mass is convective. As the Sun reaches the ZAMS (point A), a small, short-lived convective core develops (comprising only 2% of the Sun’s mass, and lasting 0.07 Gyr): in Figure 6a this is not resolved from the initial fully convective Sun, due to the short time scale involved. For the present Sun, the surface convective region (convective envelope) comprises only 1.7% of the Sun’s mass. Note that central

hydrogen burning produces no convective core in the present Sun, due to the relatively weak temperature dependence of the  $p$ - $p$  chain (unlike higher-mass stars, where the more temperature-sensitive CNO cycle dominates, resulting in a higher temperature gradient in the core, and therefore a convective core). As the Sun approaches and climbs the RGB, the convective envelope deepens; at its maximum depth, 75% of the Sun’s mass is convective (see Fig. 6a, and Table 2). As noted in § 3.2.3, this occurs fairly low on the RGB, when the Sun’s luminosity is only  $17 L_{\odot}$ . This deep convective envelope dredges up the products of partial hydrogen burning from the outer core (see § 3.5 below); this is referred to as “first dredge-up”.

When the helium core flash ignites (point H), most of the hydrogen-exhausted core is mixed in short-lived convective regions (Thomas 1967); these are not shown in Figure 6a, since our computations “jumped over” the helium core flash, as discussed in § 3.2.3. As the Sun settles down to quiet helium core burning on the horizontal branch (point J), an appreciable convective core develops (about  $0.12 M_{\odot}$ ), due to the strong temperature dependence of the triple- $\alpha$  (and  $\alpha$ -C) burning rate. The helium convective core grows with time, because the products of helium burning, namely carbon and oxygen, have a higher opacity than helium (note that increased opacity strengthens convection). After the convective core reaches about  $0.15 M_{\odot}$ , further growth is achieved by a *semiconvective* region attached to the core, which eventually reaches out to about  $0.24 M_{\odot}$ . Semiconvection occurs in this region, rather than convection, because (1) the C- and O-enriched material inside the core has more opacity than the regions outside (which contain mostly helium), and (2) in addition, C- and O-enriched material of any given composition becomes more convectively unstable if it is moved further outwards from the core, due to the opacity increase as the temperature drops. Thus a convectively neutral region (i.e., semiconvective: on the verge of being convectively unstable) develops outside the core, with a non-uniform composition, as just enough helium is mixed downwards (and carbon and oxygen upwards) that the region becomes marginally convective.

Near the end of core helium burning, models that use the customary instantaneous convective mixing approximation exhibit “helium core breathing pulses” (HeCBP). This is a convective instability that occurs when the central helium abundance grows small ( $Y_c \lesssim 0.1$ ): when even a small amount of helium-rich material gets mixed in, it makes a relatively large fractional change in the central helium abundance, and an even larger change in the nuclear energy generation rate (which drives further convection). The standard fix was to suppress this instability in stellar models by artificially forbidding growth of the helium convective core for  $Y_c \lesssim 0.1$ . Castellani *et al.* (1985) showed that following this instability in detail resulted in a few of these “breathing pulses” and a somewhat longer helium-burning lifetime. However, it is not clear that these breathing pulses would actually occur, if one took convective and semiconvective mixing time scales into account (rather than making the usually justifiable assumption of instantaneous mixing); there are (weak) indications from observations that breathing pulses do not occur (Caputo *et al.* 1989). In our preferred solar model (Fig. 6a), we suppressed these breathing pulses, but we also checked what would happen if they did occur (see Fig. 6d). Three of these breathing pulses were then encountered, showing up in Figure 6d as short-lived spikes reaching outwards near the end of core helium burning; the helium core burning lifetime was increased by 0.028 Gyr (about 25%), and the subsequent E-AGB lifetime was reduced by 0.008 Gyr (about 35%), but there were no other major differences: the same number of helium shell flashes took place, and the final mass was the same.

For stars with masses above about  $4 M_{\odot}$ , “second dredge-up” occurs on the E-AGB, as the convective envelope penetrates through the hydrogen shell (after hydrogen shell burning is extinguished). For stars of lower mass, such as the Sun, the hydrogen-burning shell is not extinguished on the E-AGB, and there is no second dredge-up.

On the AGB, the envelope convection reaches down from the surface almost to the hydrogen-burning shell (which in turn is very thin). The mass in the convective envelope is reduced as mass is shed from the surface. Our preferred solar model encounters four helium shell flashes on the AGB, each of which drives a

short-lived convective tongue (lasting about 300 yr) from the middle of the helium-burning shell out almost to the base of the hydrogen-burning shell: these are visible as short vertical lines in Figure 6a (the scale is not fine enough to show that they are actually separate from envelope convection; the final vertical line on the right corresponds to the final shell flash during the approach to the white dwarf stage). Immediately following each flash, the convective envelope retreats outward briefly, then reaches down deeper into the hydrogen shell before slowly retreating again; products of partial hydrogen burning are brought up to the surface, but true “third dredge-up” (defined as a penetration of the convective envelope below the bottom of the hydrogen shell and into the regions previously reached by the intershell convective tongue) does not occur. (Even for the  $\eta = 0.4$  case, where conditions for dredge-up are more favorable because of the more massive convective envelope, true third dredge-up does not occur.)

### 3.5. Solar Surface Abundance Changes

We followed the abundances of H,  $^3\text{He}$ ,  $^4\text{He}$ ,  $^7\text{Li}$ ,  $^{12}\text{C}$ ,  $^{13}\text{C}$ ,  $^{14}\text{N}$ ,  $^{16}\text{O}$ ,  $^{17}\text{O}$ , and  $^{18}\text{O}$ . During the pre-main-sequence,  $^7\text{Li}$  is depleted by a factor of 3, but there is no change in the other elements. The present Sun is observed to be depleted in  $^7\text{Li}$  by a factor of about 200 from its initial abundance (see, e.g., Grevesse 1984), but most of this depletion takes place while on the main sequence, as a result of processes which we do not consider in our model, such as meridional circulation or turbulence induced by rotation and (to a lesser extent) diffusion and main-sequence mass loss (see, e.g., Vauclair 1988; Pinsonneault *et al.* 1989; Michaud & Charbonneau 1991; Paper II).

During the first dredge-up (discussed in § 3.4) on the RGB, the convective envelope reaches deep into the Sun, reducing the remaining  $^7\text{Li}$  by over two orders of magnitude; this is largely due to dilution, but some  $^7\text{Li}$  burning also takes place as the convective envelope approaches its deepest extent. There is a slight enrichment of  $^4\text{He}$ , by about 8% (from  $Y = 0.274$  to 0.296); the enrichment of  $^3\text{He}$  is considerable, a factor of 5.7, the number ratio  $n(^3\text{He}/^4\text{He})$  increasing from 0.0004 to 0.0023. There is also an enrichment of  $^{13}\text{C}$  by a factor of 3, with  $n(^{12}\text{C}/^{13}\text{C})$  changing from 90 to 28. This  $^{13}\text{C}$  enrichment is only about half as great as that observed in solar-mass open cluster red giants by Gilroy (1989); probably the same mixing mechanism responsible for main-sequence  $^7\text{Li}$  depletion is responsible for creating the additional  $^{13}\text{C}$ . There is a minor enhancement of  $^{14}\text{N}$ , by a factor of 1.5, with  $n(\text{N}/\text{O})$  changing from 0.126 to 0.195;  $n(\text{C}/\text{O})$  decreases very slightly, from 0.603 to 0.534, while the oxygen isotope ratios change by only a few percent. All of these abundance changes are the result of dredging up the products of incomplete hydrogen burning.

There is a small depletion of  $^7\text{Li}$  (by 30%) and  $^3\text{He}$  (by 10%) on the E-AGB, as the convective envelope reaches into regions where these isotopes were destroyed. When helium shell flashes on the TP-AGB cause envelope convection to reach into the hydrogen shell, further abundance changes take place, generally similar to (but much smaller than) those occurring on the RGB. There is some further depletion of  $^7\text{Li}$  (by a factor of 3) and  $^3\text{He}$  (by 5%);  $n(^{12}\text{C}/^{13}\text{C})$  is reduced from 28 to 26, but nothing else changes by more than 0.5%.

### 3.6. The Sun’s Radial Excursions

Figure 7a presents the dramatic changes in the Sun’s radius as a function of time, for our preferred solar model (i.e., with mass-loss parameter  $\eta = 0.6$ ). The Sun contracts considerably during the pre-main-sequence phase. From the beginning of the main-sequence phase (point A) to the present (point B), it expands by about 10%; during the remaining main-sequence lifetime, it expands by a further 60%. As the Sun becomes a red giant, its radius grows enormously, eventually reaching  $166 R_{\odot}$  (i.e., 0.77 AU), further out than the present orbit of Venus (at 0.72 AU). However, since the Sun loses 28% of its mass on the RGB, and conservation of angular momentum for the planets implies that their orbital radii will vary inversely as the Sun’s mass, the orbits move outwards by a factor of  $1/(1 - 0.28)$ , namely 38%. Venus moves out to 1 AU (where Earth used to be); Earth moves out to 1.38 A.U. Thus Venus escapes being engulfed, as shown in Figure 7a.



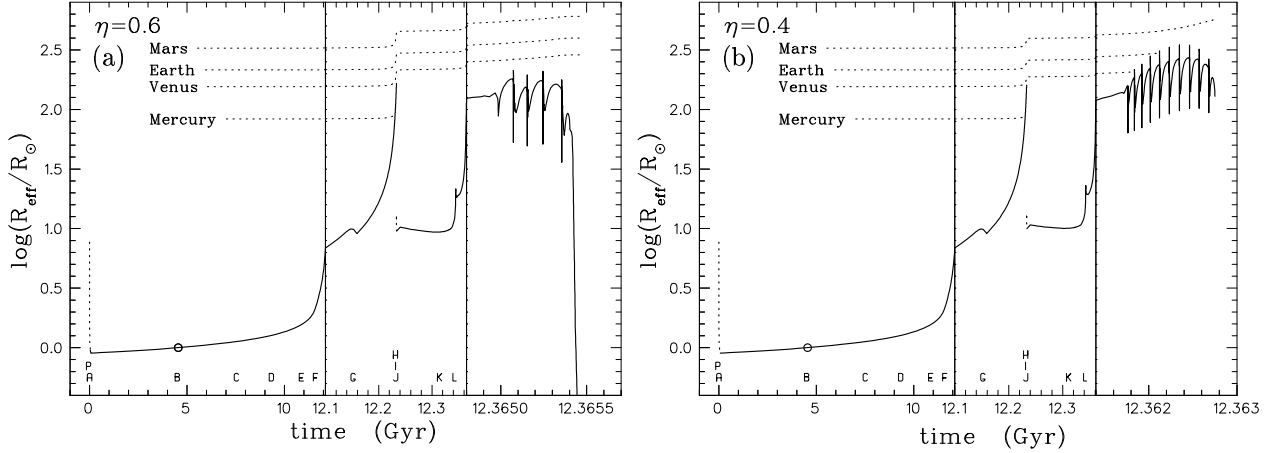


Fig. 7.—Changes in the solar radius as a function of time. (a) Our preferred mass-loss case, with  $\eta = 0.6$ ; (b) our low mass-loss case, with  $\eta = 0.4$ . The radial oscillations on the right are due to helium shell flashes. The mean orbital radii of the inner planets are also shown as a function of time (*dotted lines*); note changes in these orbital radii, due to changes in the mass of the Sun. Symbols have the same meaning as in Fig. 2.

As discussed in § 3.2.3, we “jumped over” the helium core flash which terminates the RGB (at point H), resulting in the break in the radius curve in Figure 7. During the following quiescent helium core burning on the horizontal branch, the Sun’s radius remains nearly constant, at roughly  $10 R_{\odot}$ . The radius grows rapidly at the end of core helium burning, driven by the luminosity increase at that point; after the short dip caused by the onset of the helium shell burning, the radius grows even more rapidly, as the Sun ascends the E-AGB. The Sun becomes an enormous red giant again. Just before the first helium shell flash, the Sun’s radius reaches  $180 R_{\odot}$  (i.e.,  $0.84 \text{ AU}$ ).

During a helium shell flash, the radius behaves similarly to the luminosity. First there is a rapid and deep decline (the downward spikes in Fig. 7), followed by a rapid increase (the upward spikes in Fig. 7); a slower, more moderate decline follows, and finally a still-slower increase takes place over the interflash period. This type of behavior repeats with each shell flash. Our preferred solar model reaches the largest size in its lifetime during the first helium shell flash cycle, briefly reaching a radius of  $213 R_{\odot}$  (i.e.,  $0.99 \text{ AU}$ ). However, due to the Sun’s continuing mass loss, the orbits of the planets have moved outwards sufficiently that not even Venus (now at  $1.22 \text{ AU}$ ) is engulfed, as shown in Figure 7a; note that Earth has moved out to  $1.69 \text{ AU}$  at this point. Although the peak luminosity is highest in the fourth flash (see Fig. 4), this is not true of the radius, which has begun an overall downward trend (superimposed on the flash-driven oscillations) as the Sun begins to leave the AGB (see Fig. 7a). After the fourth flash, this trend accelerates rapidly, as the Sun leaves the AGB entirely, passing through the planetary nebula stage and contracting toward the white dwarf stage. The Sun’s radius has shrunk to  $0.058 R_{\odot}$  by the time the fifth and final shell flash takes place, at an age of slightly less than  $12.4 \text{ Gyr}$ . Note that, as discussed in § 3.2.3, there is only a 10% chance that the Sun will encounter such a final shell flash; if it does not encounter a final shell flash, or after the final shell flash is over, the Sun will continue to shrink, more and more slowly, as it becomes a white dwarf.

For the extreme mass-loss case ( $\eta = 1.4$ ), the radial behavior is much the same until near the tip of the RGB; but not long after Mercury is engulfed by the expanding Sun, the Sun begins to contract rapidly as it leaves the RGB to pass through the planetary nebula stage and become a white dwarf.

For the low mass-loss case ( $\eta = 0.4$ ), the radial behavior is similar to the preferred case until helium shell flashes begin on the AGB (see Fig. 7b). However, since there is less mass loss, this solar model remains longer on the AGB, with the peak radius continuing to grow from one flash to the next until the seventh flash

is reached. Venus is engulfed on the second flash, and Earth on the fifth; a maximum radius of  $347 R_{\odot}$  (i.e., 1.61 AU) is reached during the seventh flash cycle. This is beyond the present orbit of Mars (at 1.52 AU), but by this point Mars has moved out to 2.25 AU, and escapes being engulfed (see Fig. 7*b*). After the seventh flash, peak radii become smaller, as the model begins to leave the AGB; after the tenth flash, it encounters rapid contraction toward the planetary nebula and final white dwarf stage.

#### 4. CONCLUSIONS

1. Our standard solar model has a presolar helium abundance of  $Y = 0.274$ , and metallicity  $Z = 0.01954$ ; use of the Sharp (1992) molecular opacities results in  $\alpha = 2.10$ . The base of convection is found to be at  $R_{ceb} = 0.741 R_{\odot}$ , somewhat larger (as expected from the use of Los Alamos interior opacities) than the value of  $0.713 \pm 0.003 R_{\odot}$  obtained by Christensen-Dalsgaard *et al.* (1991) from helioseismological observations. The central temperature is  $T_c = 15.43 \times 10^6$  K, resulting in predicted solar neutrino capture rates (in the absence of any MSW effect) of 6.5 SNU for  $^{37}\text{Cl}$ , and 123 SNU for  $^{71}\text{Ga}$ .

2. While on the main sequence, the Sun’s luminosity grows from  $0.7 L_{\odot}$ , 4.5 Gyr ago, to  $2.2 L_{\odot}$ , 6.5 Gyr from now. However, Kasting (1988) calculated that luminosities above about  $1.1 L_{\odot}$  (1.1 Gyr from now) would result in a “moist greenhouse” on Earth, while a true “runaway greenhouse” would occur at  $1.4 L_{\odot}$  (3.5 Gyr from now). Clouds (which he did not include in his climate model) might delay these catastrophes somewhat.

3. Our preferred Sun was based on mass loss using a Reimers (1975) wind, with a mass-loss parameter  $\eta = 0.6$ , normalized from the red giant branch (RGB) mass loss inferred from (low-mass) globular cluster horizontal branch stars. This results in a solar mass loss of  $0.275 M_{\odot}$  on the RGB, and  $0.184 M_{\odot}$  on the asymptotic giant branch (AGB), with peak mass-loss rates of 1.3 and  $2.5 \times 10^{-7} M_{\odot} \text{ yr}^{-1}$ , respectively; four helium shell flashes are encountered on the AGB, and the Sun’s final mass as a white dwarf is  $0.541 M_{\odot}$ . Since these stages will take place more than 7 Gyr in the future, we will not be able to observe them in the Sun; but solar-mass stars with similar abundances, that were formed earlier than the Sun, are going through these stages right now.

4. We also explored other mass-loss cases. For a low mass-loss case of  $\eta = 0.4$ , 10 helium shell flashes were encountered, with a final mass of  $0.576 M_{\odot}$ . We can estimate the effect of a high mass-loss case of  $\eta = 0.8$ : this case would reach the early AGB, but would not encounter any shell flashes, ending up with a white dwarf mass of about  $0.51 M_{\odot}$ . An extreme mass-loss case of  $\eta = 1.4$  never reached central helium ignition (at the tip of the RGB), and ended up as a white dwarf of  $0.434 M_{\odot}$ .

5. The Sun spends 11 Gyr on the main sequence, 0.7 Gyr traversing the HR diagram to the base of the RGB, 0.6 Gyr on the RGB, 0.1 Gyr on the horizontal branch, 0.02 Gyr on the early AGB, 0.0004 Gyr on the thermally pulsing AGB, and 0.0001 Gyr on the blueward traverse to the planetary nebula stage. The last three of these time scales depend strongly on the assumed mass loss.

(6) During the pre-main-sequence phase, surface  $^7\text{Li}$  is depleted by a factor of 3; the processes that cause main-sequence  $^7\text{Li}$  depletion were not included here. On the RGB, first dredge-up reduces  $^7\text{Li}$  by more than two orders of magnitude, due mostly to dilution as the convective envelope reaches downwards to include 75% of the Sun’s mass (there is some additional destruction of  $^7\text{Li}$  due to burning at the base of the convective envelope). Products of partial hydrogen burning are mixed to the surface:  $^4\text{He}$  is increased by 8%,  $^3\text{He}$  by a factor of 5.7,  $^{13}\text{C}$  by a factor of 3, and  $^{14}\text{N}$  by a factor of 1.5; other isotopes change relatively little. There is of course no second dredge-up in a low-mass star such as the Sun; and the considerable mass loss prevents true third dredge-up on the AGB. Nevertheless,  $^7\text{Li}$  is diluted by a factor of 4 on the AGB, and  $^3\text{He}$  is diluted by 15%; other composition changes are negligible. Note that AGB abundance changes depend on the amount of mass loss, but the RGB abundance changes are independent of mass loss, since first dredge-up occurs before mass loss becomes significant.

7. The Sun will expand enormously as it ascends the RGB, reaching  $166 R_{\odot}$ , that is, 0.77 AU, and engulfing the planet Mercury; due to the considerable RGB mass loss, the orbits of the planets move outwards (inversely to the Sun's mass), and Venus (presently at 0.72 AU) moves out to 1.0 AU and escapes being engulfed. On the AGB, when the Sun encounters thermal pulses, the Sun's radius varies periodically by a factor of 4 (with a period of about  $10^5$  yr). The peak radius reached depends on the amount of mass loss; for our preferred mass-loss case, the largest radius reached is  $213 R_{\odot}$ , that is, 0.99 AU, surprisingly close to the Earth's present orbital radius. However, at this time Venus has moved out to 1.22 AU, and Earth to 1.69 AU, both again avoiding being engulfed by the Sun. After mass loss terminates, Venus and Earth have moved out to 1.34 and 1.85 AU, respectively. (With somewhat less mass loss, Venus would be engulfed on the AGB; and even Earth would not escape for the  $\eta = 0.4$  low mass-loss case.)

8. There is a 10% chance that the Sun will encounter a final helium shell flash as it cools toward the white dwarf stage; if this occurred, this would presumably drive the Sun temporarily to higher luminosities and radii, before it resumed its descent toward the white dwarf stage.

9. The last word on the final fate of the Sun cannot be spoken until much more accurate molecular opacities and mass-loss rates are available.

We wish to thank Steven E. Koonin for the support supplied by the Kellogg Radiation Laboratory. A. I. B. wishes in addition to thank Scott D. Tremaine and Peter G. Martin for the support provided by the Canadian Institute for Theoretical Astrophysics. We wish to acknowledge helpful discussions with Silvaine Turck-Chièze and with John Bahcall, that led to our finding the bug responsible for the 1 SNU overestimate of the solar neutrino rates in our Papers I and II, namely, the 18% error in the upper  $p$ - $p$  chain branching ratio at  ${}^7\text{Be}$ . I.-J. S. is grateful to Robert F. Christy, her husband, for interesting comments and for gentlemanly help in the many tasks of daily life. We would like to thank the referee for bringing to our attention the fact that RGB lithium depletion is larger than can be accounted for by dilution alone; this led us to realize that lithium burning had taken place on the RGB. This work was supported in part by a grant from the National Science Foundation PHY-9115574, and a grant from the Natural Sciences and Engineering Research Council of Canada.

## REFERENCES

- Bahcall, J. N., & Pinsonneault, M. H. 1992*a*, Rev. Mod. Phys., 64, 885  
——— 1992*b*, ApJ, 395, L119  
Bahcall, J. N., & Ulrich, R. K. 1988, Rev. Mod. Phys., 60, 297  
Boothroyd, A. I., & Sackmann, I.-J. 1988, ApJ, 328, 653  
Boothroyd, A. I., Sackmann, I.-J., & Fowler, W. A. 1991, ApJ, 377, 318 (Paper II)  
Brown, J. A., Sneden, C., Lambert, D. L., & Dutchover, E., Jr. 1989, ApJS, 71, 293  
Caputo, F., Castellani, V., Chieffi, A., Pulone, L., & Tornambè, A. 1989, ApJ, 340, 241  
Castellani, V., Chieffi, A., Pulone, L., & Tornambè, A. 1985, ApJ, 296, 204  
Caughlan, G. R., & Fowler, W. A. 1988, Atomic Data Nucl. Data Tables, 40, 205  
Christensen-Dalsgaard, J., Gough, D. O., & Thompson, M. J. 1991, ApJ, 378, 413  
Cohen, E. R., & Taylor, B. N. 1986, Codata Bulletin No. 63 (New York: Pergamon)  
Cox, A. N., Guzik, J. A., & Kidman, R. B. 1989, ApJ, 342, 1187  
Davis, R., Jr., Lande, K., Lee, C. K., Cleveland, B. T., & Ullman, J. 1990, in *Proc. 21st International Cosmic Ray Conference*, ed. R. J. Protheroe (Adelaide: Univ. Adelaide), 155  
de Jong, T. 1983, ApJ, 274, 252  
Despain, K. H. 1981, ApJ, 251, 639

- Faulkner, J., & Swenson, F. J. 1992, ApJ, 386, L55
- GALLEX collaboration. 1992, Phys. Lett. B, 285, 376
- Gilroy, K. K. 1989, ApJ, 347, 835
- Grevesse, N. 1984, Phys. Scripta, T8, 49
- Guenther, D. B., Demarque, P., Kim, Y.-C., & Pinsonneault, M. H. 1992, ApJ, 387, 372
- Hickey, J. R., & Alton, B. M. 1983, in *Solar Irradiance Variations of Active Region Timescales*, ed. B. J. LaBonte, G. A. Chapman, H. S. Hudson, & R. C. Willson (NASA CP-2310), 43
- Hummer, D. G., & Mihalas, D. 1988, ApJ, 331, 794
- Iben, I., Jr. 1982, ApJ, 260, 821
- Iben, I., Jr., Kaler, J. B., Truran, J. W., & Renzini, A. 1983, ApJ, 264, 605
- Iglesias, C. A., & Rogers, F. J. 1991, ApJ, 371, 408
- Johnson, C. W., Kolbe, E., Koonin, S. E., & Langanke, K. 1992, ApJ, 392, 320
- Jørgensen, U. G. 1991, A&A, 246, 118
- . 1992, in *Proc. 7th Cambridge Workshop on Cool Stars, Stellar Systems, and the Sun*, ed. M. S. Giampapa & J. A. Bookbinder (San Francisco: ASP Conf. Series), 461
- Kasting, J. F. 1988, Icarus, 74, 472
- Keady, J. 1985, private communication
- Kudritzki, R. P., & Reimers, D. 1978, A&A, 70, 227
- Kurucz, R. L. 1990, private communication
- Landré, V., Prantzos, N., Aguer, P., Bogaert, G., Lefebvre, A., & Thibaud, J. P. 1990, A&A, 240, 85
- Michaud, G., & Charbonneau, P. 1991, Space Sci. Rev., 57, 1
- Mihalas, D., Däppen, W., & Hummer, D. G. 1988, ApJ, 331, 815
- Mihalas, D., Hummer, D. G., Mihalas, B. W., & Däppen, W. 1990, ApJ, 350, 300
- Mikheyev, S. P., & Smirnov, A. Yu. 1986, Nuovo Cimento C, 9, 17
- Pinsonneault, M. H., Kawaler, S. D., Sofia, S., & Demarque, P. 1989, ApJ, 338, 424
- Proffitt, C. R., & Michaud, G. 1991, ApJ, 380, 238
- Reimers, D. 1975, in *Problems in Stellar Atmospheres and Envelopes*, ed. B. Bascheck, W. H. Kegel, & G. Traving (New York: Springer), 229
- Renzini, A. 1981, in *Effects of Mass Loss on Stellar Evolution*, ed. C. Chiosi & R. Stalio (Dordrecht: Reidel), 319
- Sackmann, I.-J., & Boothroyd, A. I. 1991, ApJ, 366, 529
- Sackmann, I.-J., Boothroyd, A. I., & Fowler, W. A. 1990, ApJ, 360, 727 (Paper I)
- Sharp, C. M. 1992, A&AS, 94, 1
- Thomas, H.-C. 1967, Z. Astrophys., 67, 420
- Ulrich, R. K., & Rhodes, E. R., Jr. 1983, ApJ, 265, 551
- Vauclair, S. 1988, A&A, 335, 971
- Wasserburg, G. J., Papanastassiou, D. A., and Lee, T. 1980, in *Early Solar System Processes and the Present Solar System* (Bologna: Corso Soc. Italiana de Fisica)
- Wasserburg, G. J., Tera, F., Papanastassiou, D. A., & Huneke, J. C. 1977, Earth Planet. Sci. Lett., 35, 294
- Willson, R. C., Duncan, C. H., & Geist, J. 1980, Science, 207, 177
- Willson, R. C., & Hickey, J. R. 1977, in *The Solar Output and its Variation*, ed. O. R. White (Boulder: Colorado Associated Univ. Press), 112
- Wolfenstein, L. 1978, Phys. Rev. D, 17, 2369